https://doi.org/10.5194/egusphere-2025-1994
Preprint. Discussion started: 14 May 2025

Observations of ocean currents and turbulent mixing in the Dotson Ice Shelf cavity

Maren Elisabeth Richter[1], Karen Joy Heywood[1], and Rob Alan Hall[1]

[1]Centre for Ocean and Atmospheric Sciences, School of Environmental Sciences, University of East Anglia, Norwich, NR4 7TJ, United Kingdom

Correspondence: Maren Elisabeth Richter (m.richter@uea.ac.uk)

Abstract. Dotson Ice Shelf (DIS) is located in the Amundsen Sea sector of Antarctica, an area of rapid glacial mass loss due to ocean-driven basal melting. Here warm Circumpolar Deep Water is transported onto the continental shelf and can access ice shelf cavities and deep grounding lines, causing melting and glacial retreat and thus sea level rise. The circulation of this warm water and the heat transport within ice shelf cavities remains mostly unknown. We present observations of ocean currents, turbulent kinetic energy dissipation rate (ε) from microstructure measurements, and heat flux calculations from over 100 km of dive tracks along the seabed under DIS using an autonomous vehicle, AutoSub Long Range. We find low rates of background mixing with $\varepsilon \approx 10^{-10}\ W\ kg^{-1}$ and patches of higher mixing with $\varepsilon \approx 10^{-8}\ W\ kg^{-1}$. Higher turbulent kinetic energy dissipation rate is associated with stronger along-slope currents, high vertical current shear and positive temperature anomalies. Average vertical heat fluxes are on the order of $0.1\ W\ m^{-2}$ and maximum heat fluxes reach $52\ W\ m^{-2}$. Turbulent mixing is higher in the fast-flowing inflow region and over rough topography. We show a highly complex spatial pattern of turbulent mixing and of bottom topography, currently not resolved in bathymetry products or models of ice-shelf–ocean interactions. However, the levels of turbulent mixing experienced by the warm mCDW inflow to the DIS will lead to negligible loss of heat during its path to the grounding line, leaving plenty of heat available to melt the ice shelf base there.

1 Introduction

Dotson Ice Shelf (DIS) is located on the southern boundary of the Amundsen Sea, an area where the West Antarctic Ice Sheet is losing mass, largely driven by increasing ocean heat flux toward and beneath ice shelves. DIS contributes disproportionately to the total Amundsen Sea ice mass loss (Rignot et al., 2019). Most of the change to DIS between 1997 to 2021 was driven by thinning (Greene et al., 2022), signifying basal mass loss. Approximately 80% of the mass loss of DIS and the neighbouring Crosson Ice Shelf is through basal melting, about 20% more than the average contribution of basal mass loss in the Amundsen Sea sector (Depoorter et al., 2013). Basal melt contributes more to mass loss at DIS than at Thwaites and Pine Island Glacier Ice Shelves (basal melt contributes 53% and 65% to these ice shelves total mass loss, respectively, Depoorter et al. (2013)). Between 1979 and 2017 DIS contributed $0.6\,\mathrm{mm}$ to global eustatic sea level rise, and the rate of discharge across its grounding line has increased throughout the satellite record (Rignot et al., 2019).

https://doi.org/10.5194/egusphere-2025-1994
Preprint. Discussion started: 14 May 2025

Basal melt in the Amundsen Sea is driven by the intrusion of warm modified Circumpolar Deep Water (mCDW) onto the continental shelf where it can flow into ice shelf cavities. There it can cause melting at the grounding line, leading to basal mass loss and grounding line retreat. At DIS, there is suggested to be a strong seasonality in the velocity and heat content of the inflow and in the velocity and meltwater content of the outflow, with maximum inflows in summer and maximum outflows in autumn (Yang et al., 2022). This seasonality, as well as interannual variability at DIS, are hypothesised to be driven by local winds and sea-ice conditions (Yang et al., 2022; Kim et al., 2021).

Input of meltwater from ice shelves influences the local and global ocean circulation and climate (Hellmer, 2004; Silvano et al., 2018; Bronselaer et al., 2018), as well as sea-ice formation and persistence (Hellmer, 2004; Richardson et al., 2005; Bintanja et al., 2013; Bronselaer et al., 2018). Thus, it has important effects on ocean heat and carbon storage and transport (Silvano et al., 2018). Increased meltwater input leads to decreased winter mixing and thus to easier access of warm deep water to the Amundsen Sea ice shelves, causing further melting (Silvano et al., 2018). All these effects are modulated by the depth at which meltwater is injected into the ocean. This in turn is influenced by where melt predominantly occurs. For DIS, melt occurs at the grounding line (Khazendar et al., 2016), in outflow channels along the underside of the ice shelf (Gourmelen et al., 2017), and in locations spread inhomogeneously over the entire ice shelf base in highly complex patterns (Wåhlin et al., 2024a). Flow in the western DIS is intensified at the ice base with observed melt rates consistent with shear driven turbulence and heat transport. The central and eastern areas of DIS show low flow speeds close to the ice base and low meltwater concentrations (Wåhlin et al., 2024a). The spatial distribution of ice shelf melt has an important effect on ice shelf stability: melting concentrated at the grounding line leads to stronger grounding line retreat (Walker et al., 2008); and melting concentrated in channels may lead to weakening and break up of the floating ice shelf (Gourmelen et al., 2017).

The input of meltwater to the Amundsen Sea is also important for biological activity in the region. The flow of mCDW along the seafloor on its way into the DIS cavity enriches the mCDW in dissolved iron and manganese while the meltwater from the ice shelf itself is a source of particulate iron and manganese (van Manen et al., 2022). The addition of glacial meltwater makes the outflowing mCDW more buoyant than the dense mCDW infow, transporting iron and manganese to the surface ocean (van Manen et al., 2022) where they are important micronutrients for primary producers (Twining and Baines, 2013).

Meltrates can be highly variable in time and space, even under a single ice shelf (e.g. Davis et al., 2018; Gourmelen et al., 2017). To study where heat from mCDW interacts with the ice shelf and thus releases meltwater, we need to understand the transport and mixing processes between mCDW and overlying colder and fresher water masses within the cavity. The turbulent kinetic energy dissipation rate, ε, is the rate at which molecular viscosity dampens turbulence generated at large scales by e.g. vertical or lateral shear, and is used to quantify turbulent mixing. Due to the remote location and difficult access to cavities, this is only now starting to become feasible. To our knowledge there exist two published studies of mixing in an ice-shelf cavity, one under Pine Island Glacier (Kimura et al., 2016), and one under the Filchner Ronne Ice Shelf (Davis et al., 2022). We present a third such study, targeting DIS. We investigate the circulation and mixing in the mCDW inflow close to the bed of the cavity, quantify the upward heat transport which cools the mCDW before it can reach the grounding line and transport heat to the ice shelf base, and investigate drivers for the observed mixing.

https://doi.org/10.5194/egusphere-2025-1994
Preprint. Discussion started: 14 May 2025

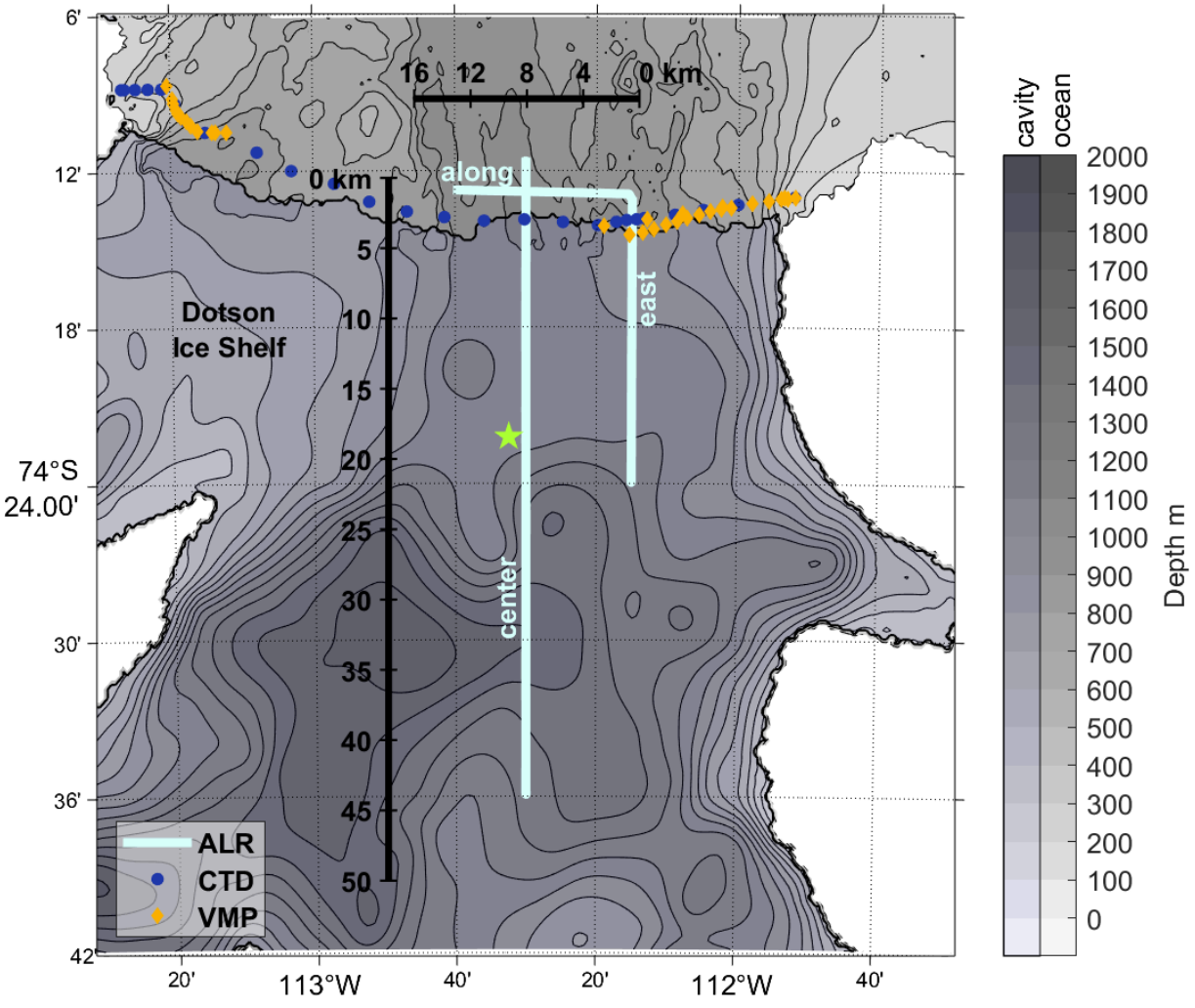

Figure 1. Map of Dotson Ice Shelf cavity and surroundings, with locations of data sets. AutoSub Long Range (ALR) dive tracks (light blue), Conductivity-Temperature-Depth (CTD) casts (dark blue circles), Vertical Microstructure Profiler (VMP) casts (orange diamonds), and the location of a CTD cast through the DIS into the cavity below (green star). Bathymetry is from Bedmachine V3 (Morlighem, 2022), with different grey scales for depths within and outside the cavity. The black line denotes the ice shelf front.

https://doi.org/10.5194/egusphere-2025-1994
Preprint. Discussion started: 14 May 2025

dive	start time	end time	duration (h)	distance (km)
centre_short	21.01.2022 06:50	22.01.2022 00:27	17.6	41
centre_long	02.02.2022 05:46	04.02.2022 01:06	43.3	91
east	05.02.2022 07:17	06.02.2022 02:40	19.4	41
along	06.02.2022 07:55	06.02.2022 14:05	6.2	13

Table 1. Metadata for the four successful dives performed by the ALR. Distance is the total length of the track summing both into and out of the cavity (or the length of the dive track along the ice shelf front for the "along" mission).

2 Data and methods

In 2022 DIS was surveyed with Conductivity, Temperature, Depth profilers (CTD), Lowered Acoustic Doppler Current Profilers (LADCP) and Vertical Microstructure Profilers (VMP) at the ice shelf front and several dive tracks into the ice shelf cavity using an AutoSub Long Range (ALR) underwater vehicle (Figure 1). The ALR travelled along the bottom of the cavity, keeping a distance of $100\,\mathrm{m}$ from the seabed. It was equipped with a Rockland Scientific International (RSI) MicroRider carrying two microstructure shear probes and two fast-response thermistors. It also carried an upward and a downward looking ADCP and Seabird Electronics temperature, conductivity, pressure, and oxygen sensors. The ALR performed four successful missions (Table 1). Of these, all except the centre_long mission had successful microstructure measurements. Centre_long does however provide valuable information on currents and hydrography in the central cavity. A clock offset between the ALR CTD and the MicroRider was resolved by calculating lagged correlations between the MicroRider pressure sensor and the CTD pressure sensor to find the offset, then correcting for the identified clock drift.

The ALR ADCP data were collected at $1\,\mathrm{s}$ frequency in twelve vertical $8\,\mathrm{m}$ bins and were processed with modified code from Eleanor Frajka-Williams' GitHub page (https://github.com/eleanorfrajka/alr_processing_dynopo), which builds on Rick Pawlowicz's RDADCP functions (https://www-old.eoas.ubc.ca/~rich/#RDADCP). The ADCP delivered good quality measurements up to $50\,\mathrm{m}$ from the ALR. To decrease noise in the ADCP data and to make displaying the data easier we show 2-minute and 10-minute temporal medians of the ADCP velocities. In cases where information on the vertical shear is not required, we additionally took a vertical median of the ADCP bins. A spectral analysis of the ADCP current velocities showed no signal at tidal frequencies, thus, we chose not to detide them. Further, the Bedmachine V3 (Morlighem, 2022) bathymetry product used to generate the CATS2008 v2023 tide model (Erofeeva et al., 2024) show water depths several hundred metres different to those measured by the ALR. We calculated the directional gradient of the Bedmachine V3 bathymetry to derive across and along isobath velocity components, and provide a measure of the steepness of the topography. For this we upsampled the Bedmachine bathymetry from its native $500\,\mathrm{m}$ resolution (Morlighem, 2022) to a denser $10\,\mathrm{m}$ resolution by cubic interpolation. This resulted in a smooth bathymetry gradient which was then linearly interpolated onto the ALR dive track.

The shear microstructure from the ALR was processed to derive turbulent kinetic energy dissipation rate (ε) with the ODAS v4.5.1 toolbox provided by RSI, following the best practices published by Lueck et al. (2024) and used by Davis et al. (2022)

https://doi.org/10.5194/egusphere-2025-1994
Preprint. Discussion started: 14 May 2025

for their ALR mission. Turbulent kinetic energy dissipation rate is derived from shear variance using Equation 1

$$\varepsilon = \frac{15}{2}\nu\overline{\left(\frac{\partial v}{\partial x}\right)^2}. \tag{1}$$

ν is the temperature-dependent molecular kinematic viscosity of water, $\overline{\left(\frac{\partial v}{\partial x}\right)^2}$ is the variance of the velocity shear fluctuations along the path of the ALR (Osborn, 1974; Oakey, 1982). We converted raw velocity shear into physical units using the ALR speed through water ($\sim 0.6\,\mathrm{m\,s^{-1}}$), derived from the ALR ADCP water track and bottom track velocities. The shear data and the accelerometer signal recording the vehicle vibrations were high-pass filtered with a Butterworth filter, forward and backward, with a cut-off frequency of $0.25\,\mathrm{Hz}$. We calculated spectra of velocity shear over $4\,\mathrm{s}$ segments of data with $2\,\mathrm{s}$ overlap between segments. To increase signal-to-noise-ratio we averaged shear spectra over half-overlapping $32\,\mathrm{s}$ windows. This results in a turbulent kinetic energy dissipation rate every $32\,\mathrm{s}$ seconds along the ALR track equivalent to every $19.2\,\mathrm{m}$. The effect of vehicle vibrations was removed by applying the Goodman method (Goodman et al., 2006) to the shear and accelerometer data. This removes the signal in the shear spectrum that can be related to the accelerometer signal. Unlike microstructure measurements performed with a small, light-weight AUV (e.g. Kolås et al., 2022), the shear microstructure recorded on AutoSub Long Range was not critically impacted by vehicle vibrations. Broad peaks in the power spectrum of the accelerometer signal caused by vehicle motion and the AUV propeller occur at frequencies above $10\,\mathrm{Hz}$, frequencies higher than the frequencies at which the Nasmyth spectra (Nasmyth, 1970) fitted to the power spectra of the shear roll off. Smaller, narrower peaks at frequencies below $10\mathrm{Hz}$ in the accelerometer spectra are successfully removed by the Goodman method for dissipation rates above $1 \times 10^{-8}\,\mathrm{W\,kg^{-1}}$. Significant deviations from the fitted Nasmyth spectra remain for dissipation rates below 1×10^{-9} arguing that quantitative estimates of dissipation rate in very quiescent regimes are not as reliable as estimates of high dissipation rates. We are nonetheless able to resolve dissipation rates up to an order of magnitude lower than the quality threshold observed in data collected by a smaller AUV Kolås et al. (2022), and individual dive tracks show good agreement between shear spectra and Nasmyth spectra for dissipation rates lower than $1 \times 10^{-10}\,\mathrm{W\,kg^{-1}}$. Additionally, any signal in the shear spectra caused by the AUV motion, and not removed by the Goodman filter, will have minimal effects on the spatio-temporal pattern of high and low ε observed by the ALR or the qualitative assessment of these patterns which this study focusses on.

Turbulent diapycnal diffusivity κ is a measure of the vertical flux of heat and mass and was estimated following Osborn (1980) as

$$\kappa = \Gamma\frac{\varepsilon}{N^2} \tag{2}$$

where $\Gamma = 0.2$ is the mixing efficiency, a measure of the amount of available turbulent kinetic energy that is permanently converted to potential energy by turbulent mixing, which is generally set to 0.2 (Shih et al., 2005). The Brunt-Väisälä frequency N^2 was calculated from the vertical density gradient below $900\,\mathrm{m}$ (the depth range occupied by the ALR) recorded in a CTD cast through a drill hole through DIS (Wåhlin et al. (2024a, b), about $15\,\mathrm{km}$ from the ice shelf front; see green star in Figure 1 for location). The CTD cast was recorded on 7 February 2022, within 4 and 17 days and about $1\,\mathrm{km}$ to the west of the two

https://doi.org/10.5194/egusphere-2025-1994
Preprint. Discussion started: 14 May 2025

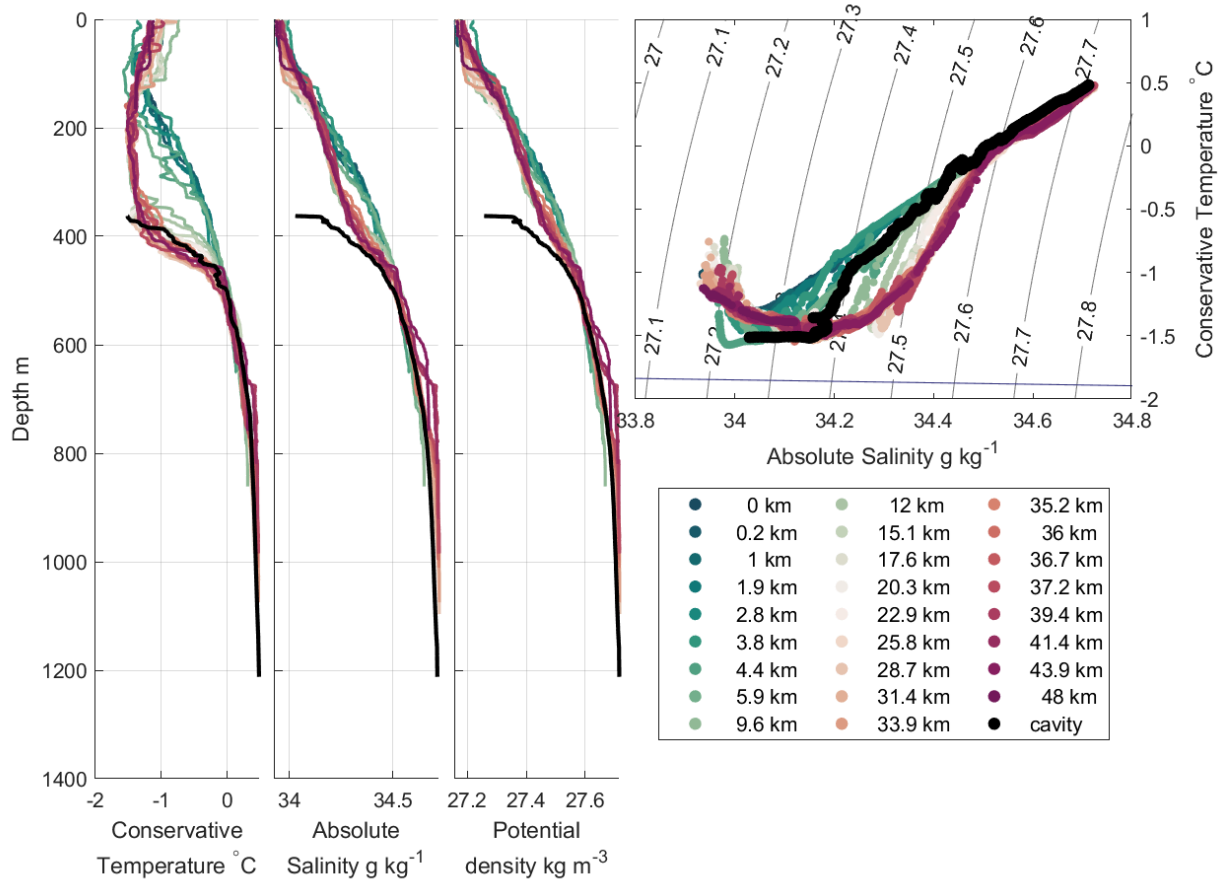

Figure 2. CTD profiles from the section along the ice shelf front as coloured lines and from the mooring location in black (see Figure 1 for locations). Profiles in the inflow region (farther east) are in reds, profiles from the outflow region (farther west) are in greens. (a) Conservative temperature, (b) Absolute salinity, (c) potential density and (d) Conservative Temperature - Absolute Salinity diagram with isopycnals in grey and freezing line in blue.

central ALR dive tracks. A constant N^2 was assumed because the density gradient is approximately linear at that depth, and also because vertical density profiles in the cavity and at the ice shelf front are similar (Figure 2).

Vertical heat Q_T and salt Q_S fluxes were calculated using Equation 3:

$$Q_T = -\rho_0 C_p \kappa \frac{\partial T}{\partial z}; \quad Q_S = -\rho_0 \kappa \frac{\partial S_A}{\partial z}; \tag{3}$$

where ρ_0 is the potential density, C_p is the specific heat capacity of seawater ($3992\,\mathrm{Jkg^{-1}K^{-1}}$), T and S are the Conservative Temperature and Absolute Salinity, respectively, and $\frac{\partial}{\partial z}$ denotes the vertical gradient.

https://doi.org/10.5194/egusphere-2025-1994
Preprint. Discussion started: 14 May 2025

Temperature changes ΔT of a seawater layer of thickness h over time t were calculated using Equation 4:

$$\Delta T = \left(\frac{Q_T}{\bar{\rho} C_P h}\right) \Delta t, \tag{4}$$

with $\bar{\rho} = 1028 kgm^{-3}$ a representative density for deep water in the DIS cavity.

Following Dotto et al. (2025) we assessed different turbulent mixing metrics in addition to ε and κ. We calculated Ertel's potential vorticity q using the approximation:

$$q \approx \left(f + \frac{\partial v}{\partial x}\right) N^2 - \left(\frac{\partial v}{\partial z}\right)\left(\frac{\partial b}{\partial x}\right), \tag{5}$$

where f is the Coriolis parameter (give number used here), v the current velocity,

$$b = -g\frac{\bar{\rho} - \rho}{\rho}, \tag{6}$$

is the buoyancy, g is the gravitational acceleration, f is the planetary vorticity, ρ is the in situ density, and $\bar{\rho} = 1028\,\mathrm{kgm}^{-3}$ is the reference density. When calculating q for the ALR data, we used the vertical distance between the good-quality bin closest to the ALR in the upward and downward looking ADCP data as Δz (approximately $38\,\mathrm{m}$), and the horizontal distance between successive two-minute medians of each bin (approximately $72\,\mathrm{m}$) as Δx. The along-slope velocity component from these bins is v. For the section at the DIS front, we used the horizontal distance between neighbouring CTD casts as Δx, the vertical resolution of the LADCP ($8\,\mathrm{m}$) as Δz, and the meridional component of the current velocity as v. We then calculated the Rossby number, Ro

$$\mathrm{Ro} \approx \frac{\frac{\partial v_{as}}{\partial x}}{f} \tag{7}$$

with the choice of v_{as} as the along-slope component of the velocity (for the currents measured by ALR) or as the northward velocity (for the ice shelf front transect), as detailed above. Ro quantifies the role of Earth's rotation relative to the vertical component of the relative vorticity.

We used N^2 and the shear measured by the ALR to calculate the dimensionless Richardson number (Ri):

$$\mathrm{Ri} = \frac{N^2}{\left(\frac{\partial u}{\partial z}\right)^2 + \left(\frac{\partial v}{\partial z}\right)^2}, \tag{8}$$

where u is the zonal velocity component. For constant N^2, Ri is low in areas of high shear. $\mathrm{Ri} < 1/4$ is a necessary condition for turbulence generated by velocity shear (Hazel, 1972; Miles, 1961; Howard, 1961).

Instabilities can be categorised as gravitational, symmetric or centrifugal (Thomas et al., 2013). These instabilities occur when q has the opposite sign to f. Gravitational, symmetric and centrifugal instabilities convert convective available potential energy, vertical and lateral shear, respectively, into kinetic energy Haine and Marshall (1998). Following Thomas et al. (2013) we calculated ϕ_{Ri} and ϕ_c using Equation 8:

$$\phi_{Ri} = \arctan\left(-Ri^{-1}\right) \quad \text{and} \quad \phi_c = \arctan\left(-1 - \frac{1}{f}\left(\frac{\partial v_{as}}{\partial x}\right)\right). \tag{9}$$

https://doi.org/10.5194/egusphere-2025-1994
Preprint. Discussion started: 14 May 2025

Since the water column shows no density inversions in our CTD section at the DIS front and the CTD cast through the DIS, we do not observe gravitational instability. The critera for symmetric instability are

$$\phi_{Ri} < \phi_c \quad \text{and} \quad -90^\circ < \phi_{Ri} < -45^\circ \quad \text{and} \quad N^2 > 0 \quad \text{and} \quad \frac{\partial v}{\partial x}\frac{1}{f} < 0,$$

or

$$-90^\circ < \phi_{Ri} < \phi_C \quad \text{and} \quad N^2 > 0 \quad \text{and} \quad \frac{\partial v_{as}}{\partial x}\frac{1}{f} > 0.$$

The criteria for centrifugal instability are

$$-45^\circ < \phi_{Ri} < \phi_C \quad \text{and} \quad N^2 > 0 \quad \text{and} \quad \frac{\partial v_{as}}{\partial x}\frac{1}{f} < 0.$$

To support the measurements by the ALR, we additionally analysed microstructure profiles along the ice shelf front measured with a RSI Vertical Microstructure Profiler (VMP). The VMP was deployed from a ship moving at $\sim 0.5\,\mathrm{ms}^{-1}$, with the VMP continuously profiling between the sea surface and $\sim 50\,\mathrm{m}$ above the seabed. The shear microstructure from the VMP was processed following Naveira Garabato et al. (2017). For details of the processing see Dotto et al. (2025). A ship-based hydrographic survey along the ice shelf front provided temperature and salinity measured with a shipboard Seabird Scientific Conductivity-Temperature-Depth (CTD) instrument and current velocity measured by a lowered Acoustic Doppler Current Profiler (LADCP). The CTD measurements were post-cruise calibrated and binned in 2-m vertical medians. Upward-looking and downward-looking LADCP measurements were processed with the LDEO_IX toolbox, incorporating information from the vessel-mounted ADCP, CTD, GPS and bottom track from the LADCP (Thurnherr, 2021). The processed data were averaged into 8-m vertical bins and detided using an updated version of the CATS2008 Antarctic tide model (Padman et al., 2002; Erofeeva et al., 2024). Conservative Temperature and Absolute Salinity were calculated using the TEOS-10 toolbox (McDougall and Barker, 2011).

3 Results and Discussion

3.1 The Dotson embayment and ice shelf front

During our observations, the DIS front is characterized by relatively warm and fresh surface waters in the upper $100\,\mathrm{m}$, a layer of colder Winter Water (WW) at $100\,\mathrm{m}$–$400\,\mathrm{m}$, and warmer, saltier mCDW below that (Figure 3a). Below the WW temperature minimum, the water column is salt-stratified with fresher colder water overlying warm salty water. The ice shelf draft is approximately $300\,\mathrm{m}$ at the front, meaning that typically only mCDW can enter the cavity. There is a bottom intensified southward inflow to the cavity in the east between the $400\,\mathrm{m}$ and $900\,\mathrm{m}$ isobaths, and a shallower, bottom intensified northward outflow in the west (Figure 3b). The outflow region is not the focus of this paper and is discussed in detail by Dotto et al. (2025). The ALR measurements just skim the western edge of the inflow. Turbulent kinetic energy dissipation rate below $500\,\mathrm{m}$, measured by the VMP, shows high values ($\approx 10^{-8}\,\mathrm{W\,kg}^{-1}$)) and the LADCP reveals a bottom intensified southward inflow (Figure 3c). The centre of the ice shelf front did not have VMP measurements, however, the ALR and the VMP measurements

https://doi.org/10.5194/egusphere-2025-1994
Preprint. Discussion started: 14 May 2025

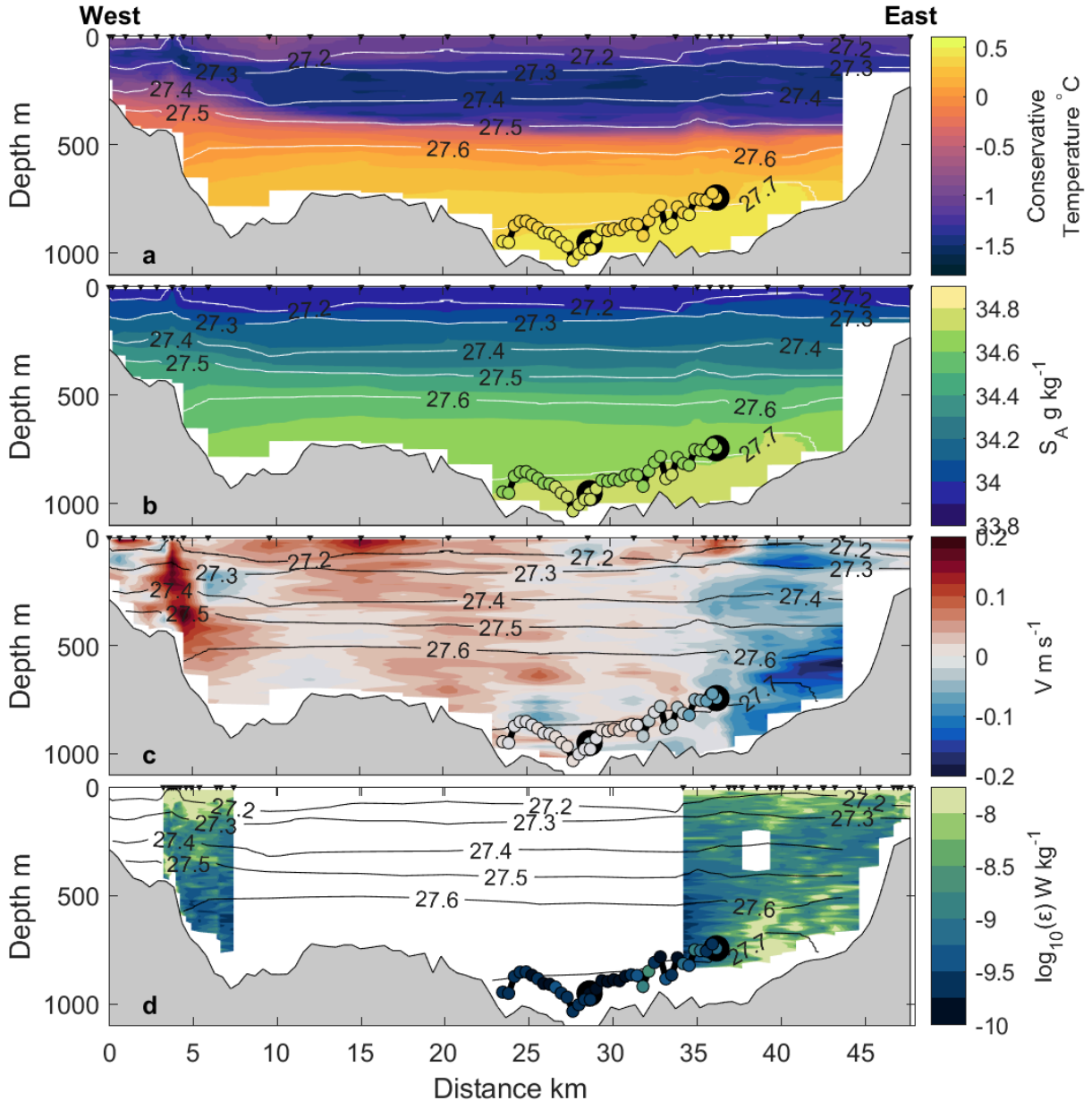

Figure 3. Sections along the DIS front of Conservative Temperature (a), Absolute Salinity (b), meridional velocity (c), and turbulent kinetic energy dissipation rate (ε (W kg^{-1}) (d). The view is out of the cavity, distance is from the western edge of the transect. Black contours show potential density. The small triangles at the top of the panels show the location of the measurements. The black line shows the track of the ALR parallel to the ice shelf front and values measured by the ALR are shown as coloured dots. The dots with bold outlines show the starting locations of the ALR dive tracks into the cavity. The bathymetry is from Bedmachine V3 (Morlighem, 2022).

https://doi.org/10.5194/egusphere-2025-1994
Preprint. Discussion started: 14 May 2025

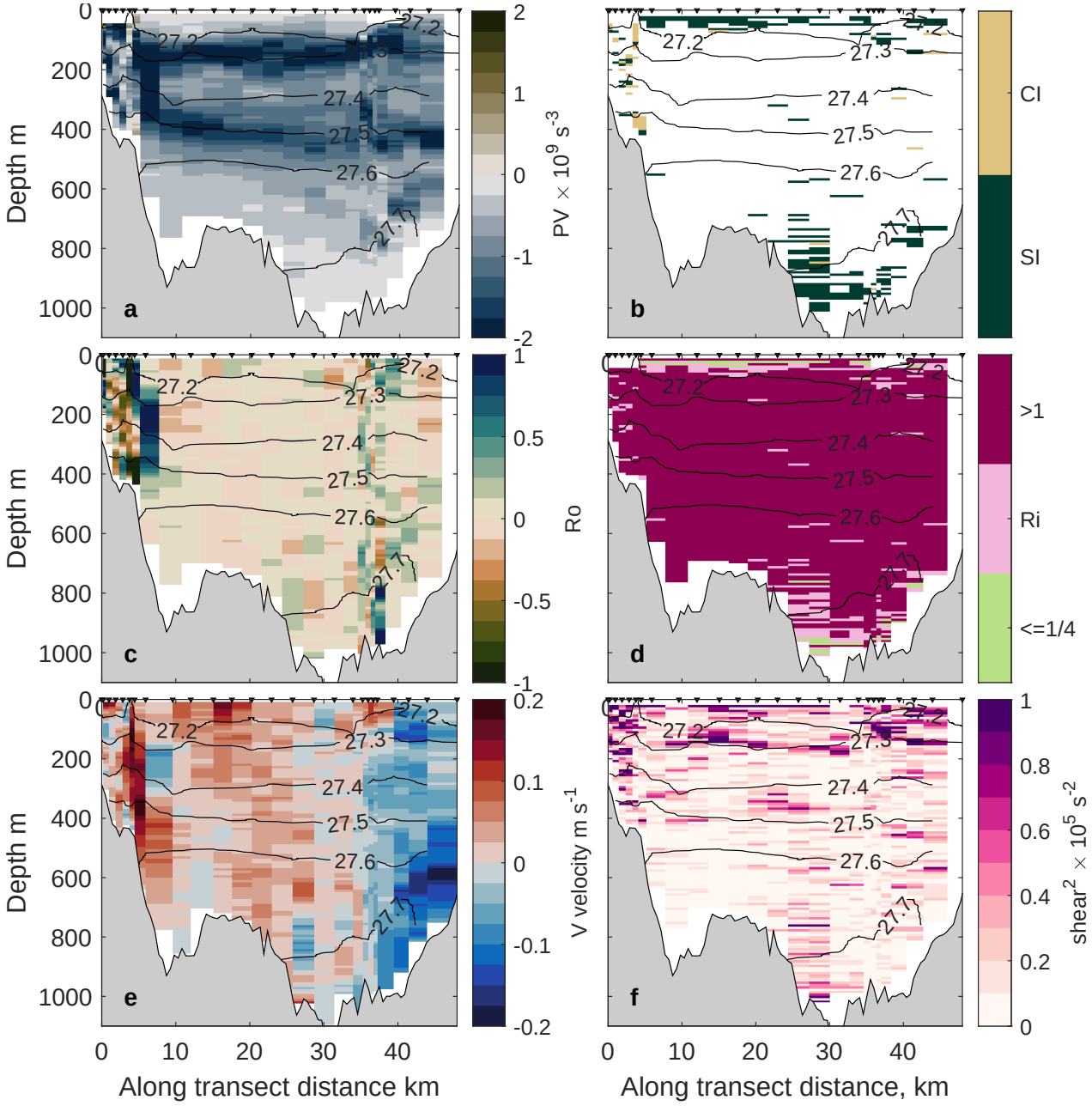

Figure 4. Instability criteria of the flow at the ice shelf front. All panels are looking out of the cavity. (a) Ertel's potential vorticity q; (b) classification of instability following Thomas et al. (2013), SI = symmetric instability, CI = centrifugal instability; (c) Rossby number; (d) Richardson number, values $< 1/4$ indicate conditions favourable for mixing driven by vertical shear, values > 1 indicate conditions not favourable for shear driven mixing; (e) meridional velocity from LADCP measurements; (f) vertical shear squared. Triangles above panels show locations of CTD/LADCP profiles. Bathymetry as for Figure 3. The black lines show potential density.

https://doi.org/10.5194/egusphere-2025-1994
Preprint. Discussion started: 14 May 2025

farthest from the lateral walls suggest that turbulence is low here. In the area where we have both VMP and ALR measurements of turbulent kinetic energy dissipation rate, both instruments record values of the same order of magnitude. This means that the ALR measurements under DIS can be interpreted with confidence as comparable in quality to the VMP measurements.

We investigate the stability of the flow at the ice shelf front (Figure 4). Potential vorticity q is almost uniformly negative, with very low values above and below the Winter Water at $200\,\mathrm{m}$ and $400\,\mathrm{m}$ depth (Figure 4a). This is mainly driven by the strong stratification above and below the WW layer. The inflow and outflow regions show high absolute values of Ro (Figure 4c) indicating high lateral shear. Following Thomas et al. (2013) we classify instabilities here as symmetric (in the inflow region) and as symmetric and centrifugal (in the outflow region) (Figure 4b). Symmetric instability is driven by high vertical current shear (Figure 4f) and thus low Richardson number (Figure 4d). The region of high turbulent kinetic energy dissipation rate ε in the inflow (Figure 3d) coincides with the patch of $R_i < 1/4$ captured at $40\,\mathrm{km}$ (Figure 4d). Ri is less than 1/4 indicating conditions favourable to turbulent mixing. Turbulent kinetic energy dissipation rate is larger than 10^{-8} here, one to two orders of magnitude higher than the background value (Figure 3d). Dotto et al. (2025) found similar results for the outflow of DIS. In our study, as in the results of Dotto et al. (2025), areas of high mixing show Ri $< 1/4$ and the instabilities are classified as symmetric or centrifugal, with no gravitational instabilities observed.

Our observations show turbulent mixing to be patchy, bottom intensified and to coincide with bathymetric features, regions of high vertical current shear and high velocities (Figures 3 and 4). The inflow shows elevated turbulent kinetic energy dissipation over a larger area than the outflow (Figure 3). However, measures of vertical and horizontal current shear are generally lower in the inflow than in the outflow (Ro and shear^2 in Figure 4). Nonetheless, the Richardson number is low close to the seabed in the inflow, and we detect conditions favourable to symmetric instability. At the nearby Pine Island Ice Shelf (PIIS) Naveira Garabato et al. (2017) found no bottom intensified inflow to the eastern cavity and no corresponding bottom intensified rate of turbulent kinetic energy dissipation from ADCP and VMP transects performed along the calving front. At the PIIS front high rates of turbulent kinetic energy dissipation below the WW were mostly confined to the outflow (Naveira Garabato et al., 2017). This may be due to the deeper ice shelf draft of the PIIS ($\approx 400\,\mathrm{m}$) compared with the DIS ($\approx 350\,\mathrm{m}$). The ice shelf draft induces a barotropic jump and limits barotropic inflow to the cavity (Wåhlin et al., 2020), thus decreasing inflow current velocities and possibly turbulent mixing. In the centre of the DIS front we observe a small region of southward current and elevated vertical and lateral current shear (at $25\,\mathrm{km}$ in Figure 4). We do not have VMP measurements in the centre of the DIS front and thus can not say with certainty what the turbulence response is. The ALR did not observe a strong southward flow or high turbulent kinetic energy dissipation rate close to the seabed here, but the ALR was not coincident in time with the LADCP measurements. Thus there may be transient patches of high turbulent kinetic energy dissipation rate here which we did not observe. Nonetheless, low values of the Richardson number and the conditions conductive to symmetric instability suggest that there may be areas of high turbulent kinetic energy dissipation outside of the main inflow and outflow branches. These might have noticeable local effects (e.g. stirring up sediment) but are unlikely to influence the major circulation within the cavity.

https://doi.org/10.5194/egusphere-2025-1994
Preprint. Discussion started: 14 May 2025

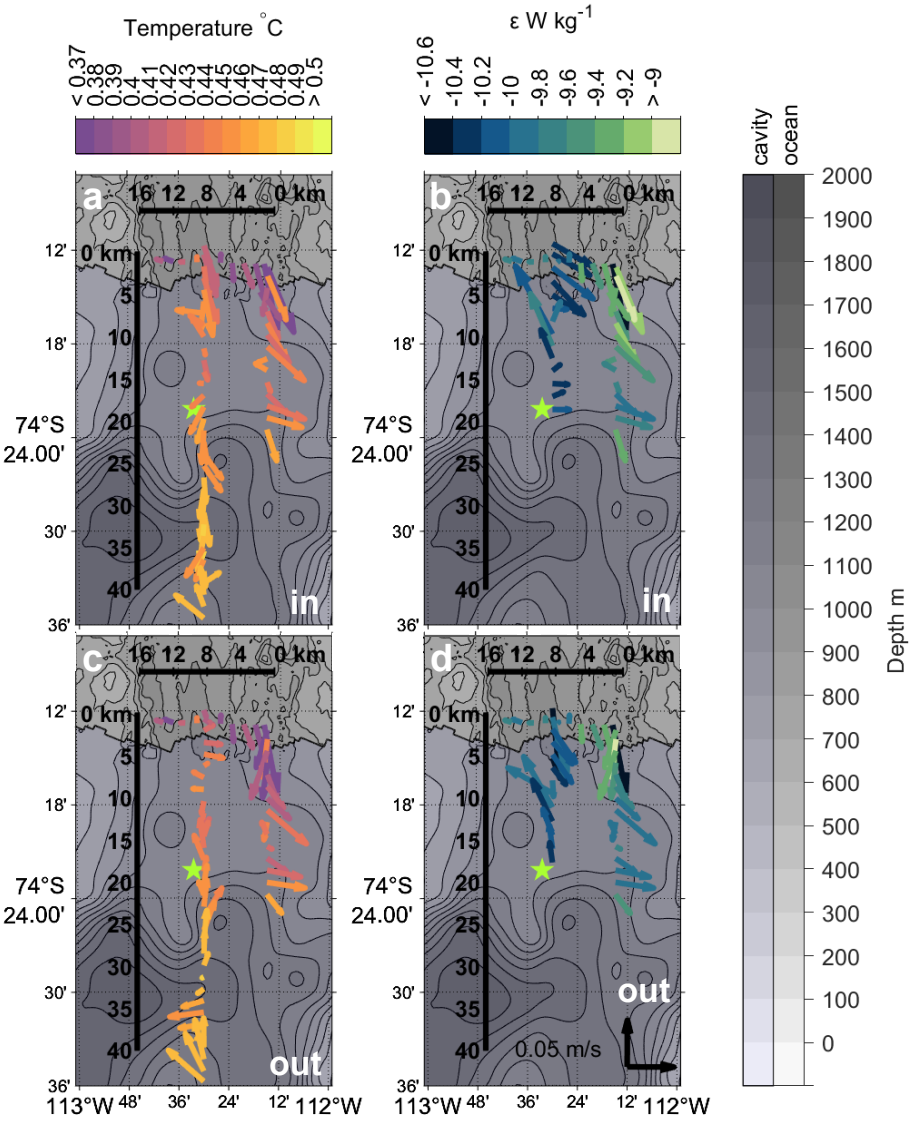

Figure 5. ALR dive tracks in front of and beneath Dotson Ice Shelf. 40-minute median depth averaged (median) currents along the dive tracks during the way into the cavity (a,b) and out of the cavity (c,d) coloured by conservative temperature (a,c) and turbulent kinetic energy dissipation rate (b,d). Star marks the location of a CTD profile obtained through a hole melted through the ice shelf into the cavity. Bathymetry as for Figure 1.

https://doi.org/10.5194/egusphere-2025-1994
Preprint. Discussion started: 14 May 2025

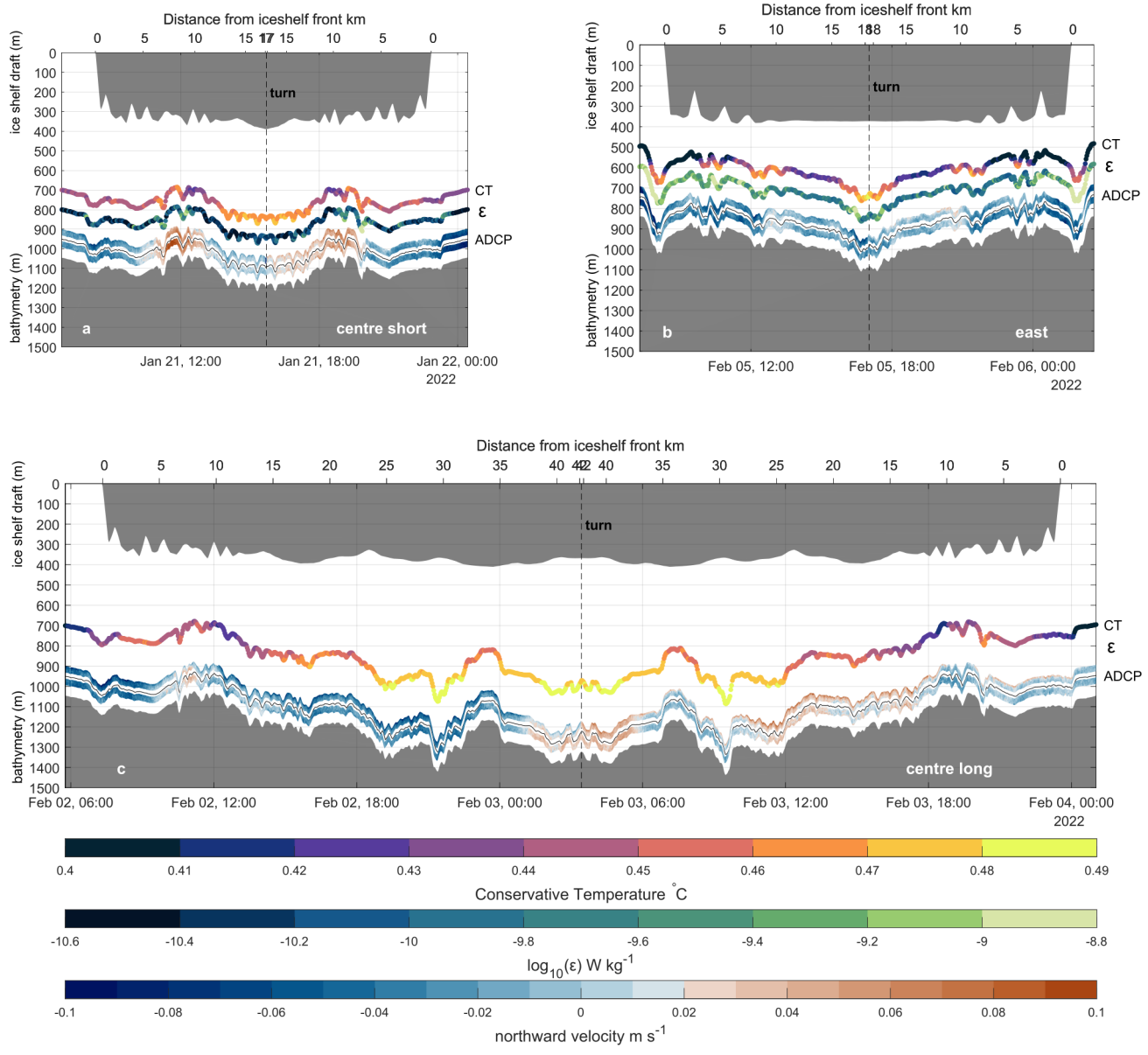

Figure 6. ALR dive tracks into Dotson ice shelf cavity for the centre_short (a), east (b) and centre_long (c) missions. The depth at which the ALR was flying is shown in the thin black line; the northward ADCP current velocity is shown above and below this line. We also show turbulent kinetic energy dissipation rate (ε) and Conservative Temperature (CT) measured by ALR, but offset vertically here for clarity. No turbulent kinetic energy dissipation values are available for the centre_long mission. The small labels to the right of the coloured lines indicate the variable measured, and corresponding colour bars are below panel c. The bathymetry is as measured by the ALR, and the depth of the iceshelf base is from Bedmachine V3 (Morlighem, 2022). Vertical dashed lines indicate where the ALR turned back.

https://doi.org/10.5194/egusphere-2025-1994
Preprint. Discussion started: 14 May 2025

3.2 ALR and CTD observations in the ice-shelf cavity

3.2.1 Hydrography in the cavity

The CTD profile through the DIS at the mooring location (Figure 4, black line) displays an approximately $100\,\mathrm{m}$ thick layer with reduced salinity and density close to the ice shelf base. Below $600\,\mathrm{m}$, the water column properties inside and out of the cavity are very similar (Figure 2). The temperature profile taken through the DIS closely matches the temperature profiles in the inflow region at the ice shelf front (Figure 2). We estimate N^2 below a depth of $900\,\mathrm{m}$ to be $6 \times 10^{-7}\mathrm{s}^{-1}$, indicating weakly stable stratification. Our ALR measurements capture the western flank of the inflow into the DIS cavity, as well as some of the outflow (Figure 3). Figures 5 and 6 show the conditions in the ice shelf cavity measured by the ALR. Currents are predominantly southeastward with low vertical shear in the east dive track, and display a more mixed pattern in the two centre dive tracks. Current speeds in the cavity mostly ranged between $0.03\,\mathrm{m\,s^{-1}}$ and $0.04\,\mathrm{m\,s^{-1}}$, with maximum current speeds up to $0.11\,\mathrm{m\,s^{-1}}$ (Table 2). Current directions show evidence of bathymetric steering (Figure 5). This is particularly evident in the east dive track and around $25\,\mathrm{km}$ along the centre dive tracks (Figure 5). Water at the ice shelf front is colder but lighter than water found deeper in the cavity (Figure 6). The temperature (Figures 6 and 5) and salinity (not shown) in the cavity generally increase with depth. The highest levels of turbulent mixing occur in the inflow region at the ice shelf front and in the east dive track, decreasing into the cavity.

3.2.2 Turbulent mixing in the cavity

Very few studies have successfully measured turbulent kinetic energy dissipation rate in ice shelf cavities (e.g. Kimura et al., 2016; Davis et al., 2022), so the observations presented here are important for establishing rates of turbulent mixing that can be incorporated into numerical models of cavity circulation. The ice–ocean interface at DIS shows evidence of a highly complex and spatially variable melt regime (Wåhlin et al., 2024a) and the CTD cast through DIS showed a $100\,\mathrm{m}$ thick melt layer (Figure 2). There are indications that double diffusion and convection play a role in vertical heat and salt transport in this region of the cavity (Wåhlin et al., 2024a), and this should be investigated in future AUV microstructure missions. Our study did not target mixing and heat transport at the ice–ocean interface, or at the interface between the mCDW and the buoyant meltwater. Instead, we found evidence of a highly spatially variable pattern of turbulent kinetic energy dissipation rate close to the seabed under DIS. We find median rates of turbulent kinetic energy dissipation ε of $10^{-11} - 10^{-10}\,\mathrm{W\,kg^{-1}}$ and median rates of diapycnal diffusivity κ of $10^{-5} - 10^{-4}\,\mathrm{m^2\,s^{-1}}$. Maximum values reached $10^{-7}\,\mathrm{W\,kg^{-1}}$ (ε) and $10^{-2}\,\mathrm{m^2\,s^{-1}}$ (κ), respectively.

Areas of high turbulence coincide with regions of steep bathymetry and high along-slope current speed (Figure 7). These areas frequently exhibit positive temperature anomalies: the temperature in the turbulent patch is higher than the average temperature at that depth which indicates that warmer water is mixed upwards from below. They also coincide with areas of high vertical current shear indicated by the high ADCP velocities and low Richardson number (Figure 7). The relationship between high turbulent kinetic energy dissipation rate, high along-slope velocity, higher than average temperature and elevated current shear is most pronounced in the east dive track (Figure 7). The centre_short and along dive tracks (Figures 5 and 6)

https://doi.org/10.5194/egusphere-2025-1994
Preprint. Discussion started: 14 May 2025

show much weaker connections between these variables, possibly influenced by the overall lower turbulent kinetic energy dissipation rate and current speeds encountered at those locations. Ri is generally greater than $1/4$ in the cavity, but it is less than $1/4$ along the east dive track in the area of high turbulent kinetic energy dissipation rate observed at $-1\,\mathrm{km}$ from the ice shelf front (Figure 7). In areas of high turbulent kinetic energy dissipation rate, we find high absolute values of q (positive and negative q occurs), and both symmetric and centrifugal instability (not shown). None of the variables associated with high turbulent kinetic energy dissipation rate (higher temperatures, high shear, high along-slope flow) are sufficient conditions for high turbulence. Additionally, no single parameter used to describe the potential for turbulence occurring (Ri, q, Ro, the stability criteria from Thomas et al. (2013)) is able to fully describe the pattern of turbulent kinetic energy dissipation rate we observe. Turbulence is patchy, episodic, and likely to be caused by a combination of factors.

The current direction relative to the bathymetric slope is seen to be important among the parameters indicative of high turbulence (Figure 7). Regions of high turbulent kinetic energy dissipation rate coincide with areas of high along-slope current speed. We are limited in our resolution of the bathymetry under Dotson, with the BedMachine V3 bathymetry (Morlighem et al., 2019; Morlighem, 2022) clearly unable to resolve small scale features in the seabed (Figure 7). The effect of bathymetry on rates of turbulent kinetic energy dissipation is clearest in areas where the bathymetry from BedMachine, used to calculate the bed's gradient, most closely matches the bathymetry measured by ALR (around $0\,\mathrm{km}$ on Figure 7). The bed and ice base of DIS show highly complex features related to ice shelf melt (this study and Wåhlin et al. (2024a)) which indicates the importance of combined multibeam and microstructure measurements, which should be attempted in the future. This high spatial variability and the effects of bathymetry under DIS are confirmed by the highly spatially variable turbulent kinetic energy dissipation rate found under two other ice shelves, Pine Island Ice Shelf (PIIS; Kimura et al. (2016)) and Filchner Ronne Ice Shelf (FRIS; Davis et al. (2022)).

Kimura et al. (2016) measured turbulent kinetic energy dissipation rate under PIIS in the southeastern Amundsen Sea, with their Autosub vehicle surveying with a saw-tooth pattern from the sea bed to the ice-ocean interface. In general, the PIIS cavity is very similar to the DIS cavity, both are warm cavity ice shelves with low tidal velocities and deep, rough beds. We observed similar levels of background mixing, with turbulent kinetic energy dissipation rate under DIS and PIIS between $10^{-11} - 10^{-10}\,\mathrm{W\,kg^{-1}}$. Maximum rates of turbulent kinetic energy dissipation were also comparable, with values under PIIS and DIS on the order of $10^{-7}\,\mathrm{W\,kg^{-1}}$. However, the location of the ALR dive tracks and the dive patterns under PIIS and DIS were very different. We observed our highest mixing values in the warm inflow to the cavity, whereas Kimura et al. (2016) observed the highest levels of mixing close to the grounding line and Naveira Garabato et al. (2017) did not find enhanced mixing in the PIIS inflow. Our ALR dive tracks did not reach the grounding line, and the dive tracks of Kimura et al. (2016) did not cover the inflow of the PIIS, making comparison difficult. Kimura et al. (2016) hypothesised that high (horizontal) density gradients driven by temperature differences and bathymetry can drive high levels of turbulence under PIIS. Our study shows that this is not a requirement for high levels of turbulence. The ALR dive tracks under DIS are all located in mCDW with very low vertical density and temperature gradients ($< 0.008\,\mathrm{g\,kg^{-1}}$ per $100\,\mathrm{m}$ and $< 0.03\,^{\circ}\mathrm{C}$ per $100\,\mathrm{m}$, respectively), but we nevertheless record turbulence values of the same order of magnitude as Kimura et al. (2016). This shows that even in ice shelf

https://doi.org/10.5194/egusphere-2025-1994
Preprint. Discussion started: 14 May 2025

cavities with similar far-field forcing, experiencing warm CDW inflow over a deep rough bed, and showing similar median and maximum rates of turbulent kinetic energy dissipation, the spatial distribution and drivers of the mixing can be very different.

Davis et al. (2022) measured turbulent kinetic energy dissipation rate under FRIS, a cold cavity ice shelf in the southern Weddell Sea. This study followed a square saw-tooth pattern, switching between bottom and surface tracking while maintaining a distance of at least $80\,\mathrm{m}$ from the seabed and ice shelf. This pattern is an effective way to optimise turbulence measurements while resolving the vertical structure in the cavity. FRIS experiences strong tidal forcing, the cavity has relatively low water-column thickness at the study site and the sea bed is virtually flat, whereas DIS experiences weak tidal forcing and the sea bed is rougher and deeper. Nonetheless Davis et al. (2022) recorded similar background mixing levels under FRIS as this study did under DIS, with average turbulent kinetic energy dissipation rates of $10^{-10}\,\mathrm{Wkg^{-1}}$ compared with our median values of $10^{-11} - 10^{-10}\,\mathrm{Wkg^{-1}}$. Although we see high turbulent kinetic energy dissipation rates associated with high current speeds (Figure 7 at $0\,\mathrm{km}$, $5\,\mathrm{km}$ and $7\,\mathrm{km}$)), we and Davis et al. (2022) do not find a statistically significant relationship between current speed and turbulent kinetic energy dissipation rate if using the entire dive track. Instead Davis et al. (2022) found that turbulent kinetic energy dissipation rate is elevated to values of up to $10^{-8}\,\mathrm{Wkg^{-1}}$ in areas of high vertical current shear, which matches our observations.

Davis et al. (2022) saw no increase in turbulence at the FRIS front, despite the current having to navigate a barotropic jump induced by the ice shelf draft (Wåhlin et al., 2020). At DIS we see increased rates turbulent kinetic energy dissipation close to the ice shelf front in the east dive track (Figure 6b), but not in the centre_short dive track (Figure 6a). We argue that the bathymetric feature co-located with the ice-shelf front in the east dive track and absent in the centre_short track is more likely to be the driver of turbulent kinetic energy dissipation rates at the DIS front than the barotropic jump.

Turbulent mixing observations outside an ice shelf cavity in another embayment on the West Antarctic Peninsula, Ryder Bay found turbulent kinetic energy dissipation rates on the order of $10^{-8}\,\mathrm{W\,kg^{-1}}$ above a bathymetric ridge (Scott et al., 2021), comparable to high turbulent kinetic energy dissipation rates we see above the bathymetric feature at $0\,\mathrm{km}$ in Figure 7. Enhanced mixing at ridges may be due to breaking of internal waves (e.g. Polzin et al., 1997), hydraulic control of currents flowing over steep bathymetry (e.g. Alford et al., 2013), or eddies in the wake of bathymetric obstacles (e.g. Muchowski et al., 2023). Our maximum turbulent kinetic energy dissipation rates are an order of magnitude higher than those observed under FRIS by Davis et al. (2022), even though Davis et al. (2022) report velocities almost twice as high as we see under DIS. This may be due to the rougher topography under DIS. While we see the topography vary by 10s of m per $100\,\mathrm{m}$, with troughs over $100\,\mathrm{m}$ deep, the depth of the bed in the area under FRIS observed by Davis et al. (2022) changes no more than approximately $10\,\mathrm{m}$ over the entire $9\,\mathrm{km}$ track. This study and the studies by Scott et al. (2021), Kimura et al. (2016), and Davis et al. (2022) show the need for repeat observations of turbulence over a wide variety of locations within ice shelf cavities. It additionally shows the importance of high resolution bathymetry within ice shelf cavities, with the currently available gridded products too coarse to resolve rough bathymetry that is a crucial driver of turbulent kinetic energy dissipation rates (Figure 7). Combined multibeam and microstructure observations would allow us to accurately understand and quantify the effect of rough bathymetry on flows within cavities with the intention of improving mixing parameterisations in high-resolution modelling

https://doi.org/10.5194/egusphere-2025-1994
Preprint. Discussion started: 14 May 2025

studies (e.g. Yung et al., 2024; Patmore et al., 2023) that will eventually feed into the low resolution climate models projecting future sea level rise and ice shelf collapse.

3.3 Heat and salt fluxes in the cavity

Maximum and median values of κ, Q_T and Q_S are given in Table 2. Our median values of diapycnal diffusivity (O($10^{-4}\,\mathrm{m^2\,s^{-1}}$–O($10^{-5}\,\mathrm{m^2\,s^{-1}}$)) are the same order of magnitude as globally-averaged ocean values (Waterhouse et al., 2014). The maximum values of diapycnal diffusivity in our study (O($10^{-2}\,\mathrm{m^2\,s^{-1}}$–O($10^{-3}\,\mathrm{m^2\,s^{-1}}$)) match values observed close to the seabed over rough terrain or at ridges (Waterhouse et al., 2014). Our median vertical heat fluxes are positive (upwards) and range between $0.11\,\mathrm{W\,m^{-2}}$ and $0.02\,\mathrm{W\,m^{-2}}$. This is the same order of magnitude as the median vertical heat flux measured in the mCDW under FRIS ($0.2\,\mathrm{W\,m^2}$; Davis et al. (2022)). However, due to opposing temperature gradients, our heat flux is positive (upwards), whereas the heatflux at the interface between modified Warm Deep Water and High Salinity Shelf Water under FRIS is negative (downwards). From our calculations of maximum and median temperature (Q_T) and salt fluxes (Q_S) for the centre_short and east dive tracks (Table 2), we estimate the heat that might be lost through upward vertical mixing as the warm inflow travels from the ice shelf front to the grounding line. We assume a distance of $80\,\mathrm{km}$ from the ice shelf front to the grounding line of DIS, consistent with the distances travelled by neutrally buoyant floats following the warm inflow into the DIS cavity (Girton et al., 2019). Our mean meridional velocity in the cavity is $-0.01\,\mathrm{m\,s^{-1}}$, which results in a travel time of 92 days. This is longer than the travel times of 1.5 – 2 months estimated from inflow velocities measured at moorings in front of DIS (Milillo et al., 2022; Yang et al., 2022) and from floats released into the DIS cavity (Girton et al., 2019). Our ALR dive tracks do not lie within the core of the mCDW inflow and thus our southward velocities are likely an underestimate. We use a travel time of 2 months, as suggested by Milillo et al. (2022) and Girton et al. (2019) for our calculations. Using the mean of the heat fluxes in Table 2 and Equation 4, we calculate the temperature decrease of the bottom $100\,\mathrm{m}$ of the water column in the cavity during its passage to the grounding line to be $8 \times 10^{-4}\,^{\circ}\mathrm{C}$. It would take 200 years for the temperature of the $100\,\mathrm{m}$ thick bottom layer in the cavity to decrease by $1\,^{\circ}\mathrm{C}$. This calculation demonstrates that the levels of turbulent mixing experienced by the warm mCDW inflow to the DIS will lead to negligible loss of heat during its path to the grounding line, leaving plenty of heat available to melt the ice shelf base there.

Our study and that of Dotto et al. (2025) represent summer snapshots of ocean conditions in front of and underneath DIS. Due to the suggested strong seasonality of the inflow and outflow speed, heat and meltwater content at DIS (Yang et al., 2022), and the observation that turbulent kinetic energy dissipation rate is high where current speeds are high (Figure 7), our estimates of mixing and heat transport may represent upper limits. To test this hypothesis, highly challenging wintertime observations of turbulent mixing, ocean velocity and ocean properties within ice shelf cavities are needed. ALR has the capability to remain moored at the seabed for months, periodically waking up to perform missions before lying dormant again. Such a campaign, though risky, using an AUV or ocean gliders, should be considered in order to resolve seasonal variability in turbulent mixing under ice shelves such as DIS.

https://doi.org/10.5194/egusphere-2025-1994
Preprint. Discussion started: 14 May 2025

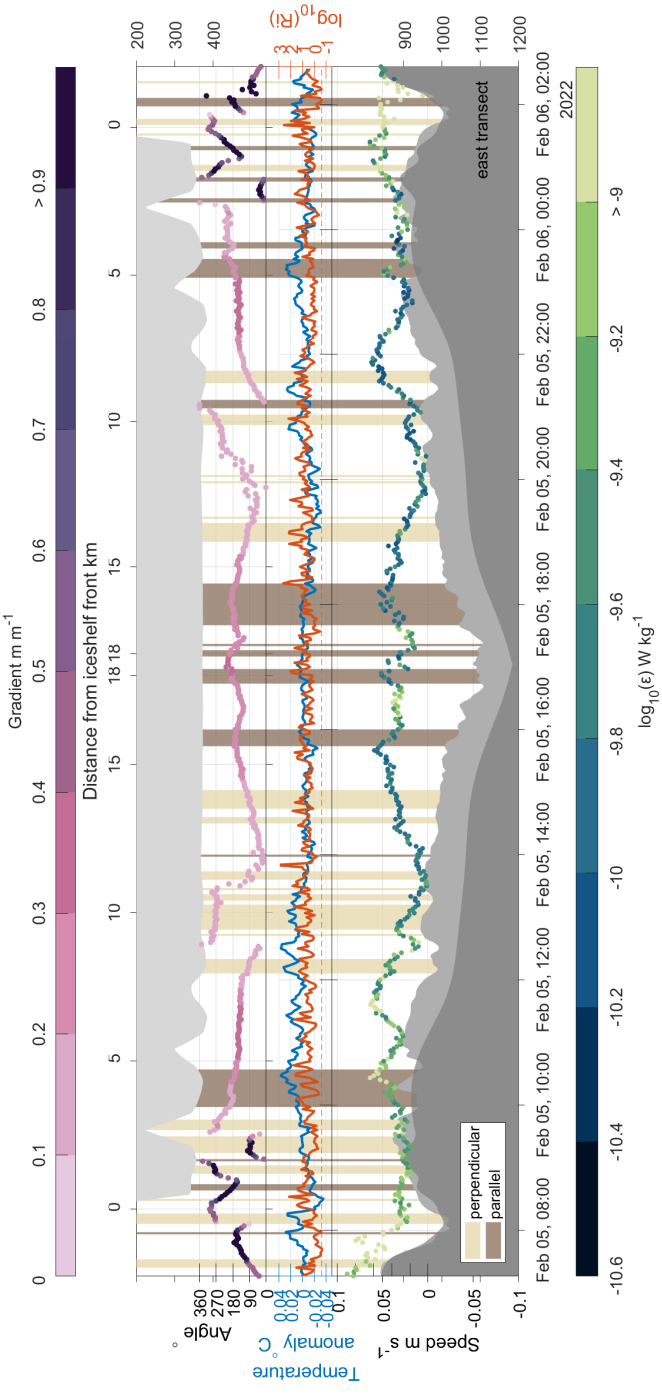

Figure 7. Timeseries of the east dive track into the Dotson Ice Shelf cavity. Top panel shows the angle at which the current direction intersects with the maximum bathymetric gradient (an angle of 0° is flow parallel to the isobaths with high ground to the right of the flow; an angle of 90° is downhill flow). Middle panel shows temperature anomaly (relative to the depth mean) and current shear. Bottom panel shows current speed coloured by turbulent kinetic energy dissipation rate, ε. Bathymetry measured by ALR is shown in light grey, and the smoothed bathymetry used to calculate the bathymetric gradient is shown in dark grey. Beige patches show where the current is perpendicular to the isobaths, and brown patches show where the current is parallel to the isobaths. The distance travelled by the ALR relative to the start of the dive track is shown on the top panel, time is shown on the bottom panel.

https://doi.org/10.5194/egusphere-2025-1994
Preprint. Discussion started: 14 May 2025

Table 2. Maximum and median values for key quantities along the east and centre_short dive tracks into the Dotson ice shelf cavity. Values are calculated from observations at their highest resolution (1 s for current speed, 32 s for all other variables), without prior smoothing or binning.

		east		centre_short	
		max	median	max	median
Current speed	ms^{-1}	0.1	0.03	0.11	0.04
ε	$\mathrm{W\,kg}^{-1}$	1.5×10^{-7}	3.3×10^{-10}	1.6×10^{-8}	5.9×10^{-11}
κ	$\mathrm{m}^2\mathrm{s}^{-1}$	0.05	1.1×10^{-4}	5.5×10^{-3}	2×10^{-5}
Qt	$\mathrm{W\,m}^{-2}$	52	0.11	5.6	0.02
Qs	$\mathrm{kg\,m}^{-2}\mathrm{s}^{-1}$	5.1×10^{-3}	1.1×10^{-5}	5.5×10^{-4}	2×10^{-6}

4 Conclusions

We have presented the first measurements of the current and turbulence regime near the seabed under the Dotson Ice Shelf. We show that turbulent kinetic energy dissipation is highly spatially variable, indicating that further effort is needed to observe, model and classify bed roughness, stratification, heat content and turbulent mixing, and their effects on melting of the ice shelf base. Background turbulent kinetic energy dissipation, outside the faster mCDW inflow, was $10^{-10}\,\mathrm{W\,kg}^{-1}$. Higher turbulent kinetic energy dissipation ($10^{-7}\,\mathrm{W\,kg}^{-1}$) coincides with the mCDW inflow, in regions of rough bathymetry, higher along slope current speed, high vertical current shear and high temperature anomalies. However, none of these drivers alone form a sufficient indicator of high turbulent kinetic energy dissipation rate. Our background $10^{-10}\,\mathrm{W\,kg}^{-1}$ and maximum $10^{-7}\,\mathrm{W\,kg}^{-1}$ rates of turbulent kinetic energy dissipation are comparable to those measured by two previous surveys under ice shelves (Kimura et al., 2016; Davis et al., 2022). Due to differences between the cavities studied and the vehicle tracks within the cavities, all three studies are able to resolve different mixing features, with the present study focussing on turbulent mixing over rough topography. We show that there are patches of elevated vertical heat flux distributed throughout the cavity, showcasing a mechanism for transporting heat from deep warm layers in the cavity toward the ice shelf base. Median values of vertical heat flux from turbulent mixing are low, showing that the mCDW in the cavity loses negligible heat on its way to the grounding line leaving plenty of heat available to melt the ice shelf base there.

Data availability. CTD and LADCP data along the ice shelf front are archived at https://doi.org/10.15784/601785 (NSF/NERC ARTEMIS and ITGC TARSAN, 2024) and https://doi.org/10.5285/18a8be08-07c6-d76c-e063-7086abc01604 (Dotto, Tiago S et al., 2024), respectively. The CTD downcast through the DIS is archived at https://doi.org/10.5878/JEJ3-KV87. All other data used in this study is archived at https://doi.org/10.5281/zenodo.15280916.

https://doi.org/10.5194/egusphere-2025-1994
Preprint. Discussion started: 14 May 2025

Author contributions. MER analysed the data, produced the figures, investigated the results, and wrote the paper. KJH and RAH acquired funding, discussed the results, and provided supervision. KJH and MER revised and edited the paper.

Competing interests. KJH is one of the co-editors-in-chief of Ocean Science.

Acknowledgements. This work is from the Thwaites-Amundsen Regional Survey and Network Integrating Atmosphere-Ice-Ocean Processes (TARSAN) project, a component of the International Thwaites Glacier Collaboration (ITGC). Support from National Science Foundation (NSF: Grant 1929991) and Natural Environment Research Council (NERC: Grant NE/S006419/1 and NE/S006591/1). Logistics provided by NSF-U.S. Antarctic Program and NERC-British Antarctic Survey. MER, KJH, and RAH were supported by TARSAN project Grant NE/S006419/1, KJH, and RAH were supported by ARTEMIS project (NE/W007045/1). We thank Tiago S. Dotto and Alberto Naveira Garabato for discussions on the VMP sections, Eleanor Frajka-Williams for the the use of her ADCP processing code and Peter E.D. Davis for support in processing the microstructure data. This is ITGC Contribution No. ITGC-145.

https://doi.org/10.5194/egusphere-2025-1994
Preprint. Discussion started: 14 May 2025

References

Alford, M. H., Girton, J. B., Voet, G., Carter, G. S., Mickett, J. B., and Klymak, J. M.: Turbulent mixing and hydraulic control of abyssal water in the Samoan Passage, Geophysical Research Letters, 40, 4668–4674, https://doi.org/10.1002/grl.50684, 2013.

Bintanja, R., van Oldenborgh, G. J., Drijfhout, S. S., Wouters, B., and Katsman, C. A.: Important role for ocean warming and increased ice-shelf melt in Antarctic sea-ice expansion, Nature Geoscience, 6, 376–379, https://doi.org/10.1038/ngeo1767, 2013.

Bronselaer, B., Winton, M., Griffies, S. M., Hurlin, W. J., Rodgers, K. B., Sergienko, O. V., Stouffer, R. J., and Russell, J. L.: Change in future climate due to Antarctic meltwater, Nature, 564, 53–58, https://doi.org/10.1038/s41586-018-0712-z, 2018.

Davis, P. E. D., Jenkins, A., Nicholls, K. W., Brennan, P. V., Abrahamsen, E. P., Heywood, K. J., Dutrieux, P., Cho, K., and Kim, T.: Variability in Basal Melting Beneath Pine Island Ice Shelf on Weekly to Monthly Timescales, Journal of Geophysical Research: Oceans, 123, 8655–8669, https://doi.org/10.1029/2018jc014464, 2018.

Davis, P. E. D., Jenkins, A., Nicholls, K. W., Dutrieux, P., Schröder, M., Janout, M. A., Hellmer, H. H., Templeton, R., and McPhail, S.: Observations of Modified Warm Deep Water Beneath Ronne Ice Shelf, Antarctica, From an Autonomous Underwater Vehicle, Journal of Geophysical Research: Oceans, 127, https://doi.org/10.1029/2022jc019103, 2022.

Depoorter, M. A., Bamber, J. L., Griggs, J. A., Lenaerts, J. T. M., Ligtenberg, S. R. M., van den Broeke, M. R., and Moholdt, G.: Calving fluxes and basal melt rates of Antarctic ice shelves, Nature, 502, 89–92, https://doi.org/10.1038/nature12567, 2013.

Dotto, T. S., Sheehan, P. M. F., Zheng, Y., Hall, R. A., Damerell, G. M., and Heywood, K. J.: Heterogenous Mixing Processes in the Dotson Ice Shelf Outflow, Antarctica, Geophysical Research Letters, https://doi.org/10.1029/2024JC022051, in production, 2025.

Dotto, Tiago S, Hall, Robert A, Heywood, Karen J, Provost, Paul, and Platt, William: Lowered Acoustic Doppler Current Profiler (LADCP) data collected in the Amundsen Sea for the TARSAN Project, January - February 2022., https://doi.org/10.5285/18A8BE08-07C6-D76C-E063-7086ABC01604, 2024.

Erofeeva, S., Greene, C. A., Howard, S. L., Padman, L., and Sutterley, T.: CATS2008_v2023: Circum-Antarctic Tidal Simulation 2008, version 2023, https://doi.org/10.15784/601772, 2024.

Girton, J. B., Christianson, K., Dunlap, J., Dutrieux, P., Gobat, J., Lee, C., and Rainville, L.: Buoyancy-adjusting Profiling Floats for Exploration of Heat Transport, Melt Rates, and Mixing in the Ocean Cavities Under Floating Ice Shelves, in: OCEANS 2019 MTS/IEEE SEATTLE, pp. 1–6, https://doi.org/10.23919/OCEANS40490.2019.8962744, 2019.

Goodman, L., Levine, E. R., and Lueck, R. G.: On Measuring the Terms of the Turbulent Kinetic Energy Budget from an AUV, Journal of Atmospheric and Oceanic Technology, 23, 977–990, https://doi.org/10.1175/jtech1889.1, 2006.

Gourmelen, N., Goldberg, D. N., Snow, K., Henley, S. F., Bingham, R. G., Kimura, S., Hogg, A. E., Shepherd, A., Mouginot, J., Lenaerts, J. T. M., Ligtenberg, S. R. M., and van de Berg, W. J.: Channelized Melting Drives Thinning Under a Rapidly Melting Antarctic Ice Shelf, Geophysical Research Letters, 44, 9796–9804, https://doi.org/10.1002/2017gl074929, 2017.

Greene, C. A., Gardner, A. S., Schlegel, N.-J., and Fraser, A. D.: Antarctic calving loss rivals ice-shelf thinning, Nature, 609, 948–953, https://doi.org/10.1038/s41586-022-05037-w, 2022.

Haine, T. W. N. and Marshall, J.: Gravitational, Symmetric, and Baroclinic Instability of the Ocean Mixed Layer, Journal of Physical Oceanography, 28, 634–658, https://doi.org/10.1175/1520-0485(1998)028<0634:gsabio>2.0.co;2, 1998.

Hazel, P.: Numerical studies of the stability of inviscid stratified shear flows, Journal of Fluid Mechanics, 51, 39–61, https://doi.org/10.1017/s0022112072001065, 1972.

https://doi.org/10.5194/egusphere-2025-1994
Preprint. Discussion started: 14 May 2025

Hellmer, H. H.: Impact of Antarctic ice shelf basal melting on sea ice and deep ocean properties, Geophysical Research Letters, 31, https://doi.org/10.1029/2004gl019506, 2004.

Howard, L. N.: Note on a paper of John W. Miles, Journal of Fluid Mechanics, 10, 509, https://doi.org/10.1017/s0022112061000317, 1961.

Khazendar, A., Rignot, E., Schroeder, D. M., Seroussi, H., Schodlok, M. P., Scheuchl, B., Mouginot, J., Sutterley, T. C., and Velicogna, I.: Rapid submarine ice melting in the grounding zones of ice shelves in West Antarctica, Nature Communications, 7, https://doi.org/10.1038/ncomms13243, 2016.

Kim, T., Yang, H. W., Dutrieux, P., Wåhlin, A. K., Jenkins, A., Kim, Y. G., Ha, H. K., Kim, C., Cho, K., Park, T., Park, J., Lee, S., and Cho, Y.: Interannual Variation of Modified Circumpolar Deep Water in the Dotson-Getz Trough, West Antarctica, Journal of Geophysical Research: Oceans, 126, https://doi.org/10.1029/2021jc017491, 2021.

Kimura, S., Jenkins, A., Dutrieux, P., Forryan, A., Naveira Garabato, A. C., and Firing, Y.: Ocean mixing beneath Pine Island Glacier ice shelf, West Antarctica: OCEAN MIXING BENEATH PIG, Journal of Geophysical Research: Oceans, 121, 8496–8510, https://doi.org/10.1002/2016jc012149, 2016.

Kolås, E. H., Mo-Bjørkelund, T., and Fer, I.: Technical note: Turbulence measurements from a light autonomous underwater vehicle, Ocean Science, 18, 389–400, https://doi.org/10.5194/os-18-389-2022, 2022.

Lueck, R., Fer, I., Bluteau, C., Dengler, M., Holtermann, P., Inoue, R., LeBoyer, A., Nicholson, S.-A., Schulz, K., and Stevens, C.: Best practices recommendations for estimating dissipation rates from shear probes, Frontiers in Marine Science, 11, https://doi.org/10.3389/fmars.2024.1334327, 2024.

McDougall, T. J. and Barker, P. M.: Getting started with TEOS-10 and the Gibbs Seawater (GSW) oceanographic toolbox, SCOR/IAPSO WG, 127, 1–28, 2011.

Miles, J. W.: On the stability of heterogeneous shear flows, Journal of Fluid Mechanics, 10, 496, https://doi.org/10.1017/s0022112061000305, 1961.

Milillo, P., Rignot, E., Rizzoli, P., Scheuchl, B., Mouginot, J., Bueso-Bello, J. L., Prats-Iraola, P., and Dini, L.: Rapid glacier retreat rates observed in West Antarctica, Nature Geoscience, 15, 48–53, https://doi.org/10.1038/s41561-021-00877-z, 2022.

Morlighem, M.: MEaSUREs BedMachine Antarctica, Version 3, https://doi.org/10.5067/FPSU0V1MWUB6, 2022.

Morlighem, M., Rignot, E., Binder, T., Blankenship, D., Drews, R., Eagles, G., Eisen, O., Ferraccioli, F., Forsberg, R., Fretwell, P., Goel, V., Greenbaum, J. S., Gudmundsson, H., Guo, J., Helm, V., Hofstede, C., Howat, I., Humbert, A., Jokat, W., Karlsson, N. B., Lee, W. S., Matsuoka, K., Millan, R., Mouginot, J., Paden, J., Pattyn, F., Roberts, J., Rosier, S., Ruppel, A., Seroussi, H., Smith, E. C., Steinhage, D., Sun, B., Broeke, M. R. v. d., Ommen, T. D. v., Wessem, M. v., and Young, D. A.: Deep glacial troughs and stabilizing ridges unveiled beneath the margins of the Antarctic ice sheet, Nature Geoscience, 13, 132–137, https://doi.org/10.1038/s41561-019-0510-8, 2019.

Muchowski, J., Arneborg, L., Umlauf, L., Holtermann, P., Eisbrenner, E., Humborg, C., Jakobsson, M., and Stranne, C.: Diapycnal Mixing Induced by Rough Small-Scale Bathymetry, Geophysical Research Letters, 50, https://doi.org/10.1029/2023gl103514, 2023.

Nasmyth, P. W.: Oceanic turbulence, phdthesis, University of British Columbia, https://doi.org/10.14288/1.0302459, 1970.

Naveira Garabato, A. C., Forryan, A., Dutrieux, P., Brannigan, L., Biddle, L. C., Heywood, K. J., Jenkins, A., Firing, Y. L., and Kimura, S.: Vigorous lateral export of the meltwater outflow from beneath an Antarctic ice shelf, Nature, 542, 219–222, https://doi.org/10.1038/nature20825, 2017.

NSF/NERC ARTEMIS and ITGC TARSAN: Vertical ocean profiles collected by a Conductivity-Temperature-Depth (CTD) package in the Amundsen Sea, https://doi.org/10.15784/601785, 2024.

https://doi.org/10.5194/egusphere-2025-1994
Preprint. Discussion started: 14 May 2025

Oakey, N. S.: Determination of the Rate of Dissipation of Turbulent Energy from Simultaneous Temperature and Velocity Shear Microstructure Measurements, Journal of Physical Oceanography, 12, 256–271, https://doi.org/10.1175/1520-0485(1982)012<0256:dotrod>2.0.co;2, 1982.

Osborn, T. R.: Vertical Profiling of Velocity Microstructure, Journal of Physical Oceanography, 4, 109–115, https://doi.org/10.1175/1520-0485(1974)004<0109:vpovm>2.0.co;2, 1974.

Osborn, T. R.: Estimates of the Local Rate of Vertical Diffusion from Dissipation Measurements, Journal of Physical Oceanography, 10, 83–89, https://doi.org/10.1175/1520-0485(1980)010<0083:eotlro>2.0.co;2, 1980.

Padman, L., Fricker, H. A., Coleman, R., Howard, S., and Erofeeva, L.: A new tide model for the Antarctic ice shelves and seas, Annals of Glaciology, 34, 247–254, https://doi.org/10.3189/172756402781817752, 2002.

Patmore, R. D., Holland, P. R., Vreugdenhil, C. A., Jenkins, A., and Taylor, J. R.: Turbulence in the Ice Shelf–Ocean Boundary Current and Its Sensitivity to Model Resolution, Journal of Physical Oceanography, 53, 613–633, https://doi.org/10.1175/jpo-d-22-0034.1, 2023.

Polzin, K. L., Toole, J. M., Ledwell, J. R., and Schmitt, R. W.: Spatial Variability of Turbulent Mixing in the Abyssal Ocean, Science, 276, 93–96, https://doi.org/10.1126/science.276.5309.93, 1997.

Richardson, G., Wadley, M. R., Heywood, K. J., Stevens, D. P., and Banks, H. T.: Short-term climate response to a freshwater pulse in the Southern Ocean, Geophysical Research Letters, 32, https://doi.org/10.1029/2004gl021586, 2005.

Rignot, E., Mouginot, J., Scheuchl, B., van den Broeke, M., van Wessem, M. J., and Morlighem, M.: Four decades of Antarctic Ice Sheet mass balance from 1979–2017, Proceedings of the National Academy of Sciences, 116, 1095–1103, https://doi.org/10.1073/pnas.1812883116, 2019.

Scott, R. M., Brearley, J. A., Naveira Garabato, A. C., Venables, H. J., and Meredith, M. P.: Rates and Mechanisms of Turbulent Mixing in a Coastal Embayment of the West Antarctic Peninsula, Journal of Geophysical Research: Oceans, 126, https://doi.org/10.1029/2020jc016861, 2021.

Shih, L. H., Koseff, J. R., Ivey, G. N., and Ferziger, J. H.: Parameterization of turbulent fluxes and scales using homogeneous sheared stably stratified turbulence simulations, Journal of Fluid Mechanics, 525, 193–214, https://doi.org/10.1017/s0022112004002587, 2005.

Silvano, A., Rintoul, S. R., Peña-Molino, B., Hobbs, W. R., van Wijk, E., Aoki, S., Tamura, T., and Williams, G. D.: Freshening by glacial meltwater enhances melting of ice shelves and reduces formation of Antarctic Bottom Water, Science Advances, 4, https://doi.org/10.1126/sciadv.aap9467, 2018.

Thomas, L. N., Taylor, J. R., Ferrari, R., and Joyce, T. M.: Symmetric instability in the Gulf Stream, Deep Sea Research Part II: Topical Studies in Oceanography, 91, 96–110, https://doi.org/10.1016/j.dsr2.2013.02.025, 2013.

Thurnherr, A. M.: How To Process LADCP Data With the LDEO Software (Version IX.14). Retrieved from https://www.ldeo.columbia.edu/~ant/LADCP.html, https://www.ldeo.columbia.edu/ ant/LADCP.html, 2021.

Twining, B. S. and Baines, S. B.: The Trace Metal Composition of Marine Phytoplankton, Annual Review of Marine Science, 5, 191–215, https://doi.org/10.1146/annurev-marine-121211-172322, 2013.

van Manen, M., Aoki, S., Brussaard, C. P., Conway, T. M., Eich, C., Gerringa, L. J., Jung, J., Kim, T.-W., Lee, S., Lee, Y., Reichart, G.-J., Tian, H.-A., Wille, F., and Middag, R.: The role of the Dotson Ice Shelf and Circumpolar Deep Water as driver and source of dissolved and particulate iron and manganese in the Amundsen Sea polynya, Southern Ocean, Marine Chemistry, 246, 104 161, https://doi.org/10.1016/j.marchem.2022.104161, 2022.

Wåhlin, A., Alley, K. E., Begeman, C., Hegrenæs, Ø., Yuan, X., Graham, A. G. C., Hogan, K., Davis, P. E. D., Dotto, T. S., Eayrs, C., Hall, R. A., Holland, D. M., Kim, T. W., Larter, R. D., Ling, L., Muto, A., Pettit, E. C., Schmidt, B. E., Snow, T., Stedt, F., Washam, P. M.,

https://doi.org/10.5194/egusphere-2025-1994
Preprint. Discussion started: 14 May 2025

Wahlgren, S., Wild, C., Wellner, J., Zheng, Y., and Heywood, K. J.: Swirls and scoops: Ice base melt revealed by multibeam imagery of an Antarctic ice shelf, Science Advances, 10, https://doi.org/10.1126/sciadv.adn9188, 2024a.

Wåhlin, A., Sjövall, A., Symons, M., Ling, L., Stedt, F., Eayrs, C., and Holland, D.: Data from AUV Ran missions during Nathaniel B. Palmer cruise NBP2202, https://doi.org/10.5878/JEJ3-KV87, 2024b.

Wåhlin, A. K., Steiger, N., Darelius, E., Assmann, K. M., Glessmer, M. S., Ha, H. K., Herraiz-Borreguero, L., Heuzé, C., Jenkins, A., Kim, T. W., Mazur, A. K., Sommeria, J., and Viboud, S.: Ice front blocking of ocean heat transport to an Antarctic ice shelf, Nature, 578, 568–571, https://doi.org/10.1038/s41586-020-2014-5, 2020.

Walker, R. T., Dupont, T. K., Parizek, B. R., and Alley, R. B.: Effects of basal-melting distribution on the retreat of ice-shelf grounding lines, Geophysical Research Letters, 35, https://doi.org/10.1029/2008gl034947, 2008.

Waterhouse, A. F., MacKinnon, J. A., Nash, J. D., Alford, M. H., Kunze, E., Simmons, H. L., Polzin, K. L., St. Laurent, L. C., Sun, O. M., Pinkel, R., Talley, L. D., Whalen, C. B., Huussen, T. N., Carter, G. S., Fer, I., Waterman, S., Naveira Garabato, A. C., Sanford, T. B., and Lee, C. M.: Global Patterns of Diapycnal Mixing from Measurements of the Turbulent Dissipation Rate, Journal of Physical Oceanography, 44, 1854–1872, https://doi.org/10.1175/jpo-d-13-0104.1, 2014.

Yang, H. W., Kim, T.-W., Dutrieux, P., Wåhlin, A. K., Jenkins, A., Ha, H. K., Kim, C. S., Cho, K.-H., Park, T., Lee, S. H., and Cho, Y.-K.: Seasonal variability of ocean circulation near the Dotson Ice Shelf, Antarctica, Nature Communications, 13, https://doi.org/10.1038/s41467-022-28751-5, 2022.

Yung, C. K., Rosevear, M. G., Morrison, A. K., Hogg, A. M., and Nakayama, Y.: Stratified suppression of turbulence in an ice shelf basal melt parameterisation, https://doi.org/10.5194/egusphere-2024-3513, 2024.